

Modeling and simulation of single nanobelt SnO₂ gas sensors with FET structure

P. Andrei^a, L.L. Fields¹, J.P. Zheng^{a,*}, Y. Cheng^b, P. Xiong^b

^a Department of Electrical and Computer Engineering, Florida A&M University and Florida State University, Tallahassee, FL 32310, United States

^b Department of Physics and Center for Materials Research and Technology (MARTECH), Florida State University, Tallahassee, FL 32306, United States

Received 12 March 2007; received in revised form 7 June 2007; accepted 7 June 2007

Available online 17 June 2007

Abstract

Individual tin dioxide nanobelts were used to fabricate field-effect transistor (FET) devices. The output characteristics of these devices have been measured under various ambient conditions, and modeled with a modified drift-diffusion model in which quantum mechanical effects are taken into consideration using the density-gradient model. It is shown that the saturation of the output curves (drain current versus drain-to-source voltage) in air is not due to channel pinch-off, but rather to the saturation of the reversed-biased current of the Schottky-like contact. In this case the source and drain contacts behave like rectifying diodes and can be modeled as two Schottky diodes connected back-to-back with a series resistance from the nanobelt separating the diodes. In the presence of hydrogen the rectifying behavior of the two contacts disappears and the current through the device is limited by the resistance of the nanobelt that can be modulated efficiently by using a gate electrode.

© 2007 Elsevier B.V. All rights reserved.

Keywords: Model; Tin dioxide nanobelts; Schottky-like contact; Field-effect transistor

1. Introduction

Because of the enormous potential for revolutionizing chemical and environmental sensing, one-dimensional semiconducting nano-structures in various forms are attracting intense research interest. Three-terminal field-effect transistor (FET) devices are one of the most researched device structures for such applications, as evidenced by the rapidly growing number of articles published on novel nano-structure sensors with FET configurations [1–12]. Among the most commonly used nano-sensing elements are tin dioxide (SnO₂) nanobelts. SnO₂ is a wide bandgap oxide semiconductor whose electrical conductivity depends sensitively on the properties of the surrounding atmosphere. In this article the current–voltage characteristics of single-nanobelt FETs are presented and modeled by using a well calibrated drift-diffusion model.

The article is structured as follows: Section 2 presents details about the fabrication and characteristics of the nanobelt sensor.

Section 3 describes the model and details of numerical implementation. Section 4 discusses the calibration technique and numerical results, which are followed by conclusions.

2. Fabrication and experimental data

The fabrication of SnO₂ nanobelt devices can be briefly described as follows: SnO powder was placed on a flat rectangular piece of alumina that was inserted in the center of an alumina tube that was inserted into a horizontal tube, where the temperature, pressure, carrier-gas flow rate, and evaporation time were controlled. Alumina substrates were placed downstream from the source powder in order to collect the deposited nanobelts. Next, the gas lines were vacuumed down to less than 25 mTorr. Then, argon gas was allowed to flow through the system at a constant rate of 50 standard cubic centimeters per minute (sccm) and the pressure was set and maintained at 300 Torr. The temperature was ramped up to 1000 °C at a rate of 20 °C/min and maintained for 2 h before ramping the temperature back to 25 °C. After thermal evaporation, a wool-like deposit of single-crystalline SnO₂ nanobelts was retrieved from the alumina substrate and separated into individual nanobelts in an isopropyl alcohol solution via ultrasonic agitation. Some SnO₂ nanobelts were dispersed

* Corresponding author. Tel.: +1 850 410 6464; fax: +1 850 410 6479.

E-mail address: zheng@eng.fsu.edu (J.P. Zheng).

¹ Present address: Optical Physics and Networks Technology, Corning Inc., Corning, NY 14831, United States.

onto a Si/SiO₂ substrate by placing a drop of the solution on it. A single nanobelt was identified with a mask aligner and photolithography was performed to define a photoresist electrode pattern on it. Pulsed laser deposition was used to deposit a thin film (~100 nm thick) of ruthenium oxide (RuO₂) onto the pattern, in order to achieve good electrical contacts to the nanobelt. RuO₂ has metal-like conductivity and adheres well to the SnO₂ nanobelts. Furthermore, in contrast to widely used contacting metals such as Cr and Ti, RuO₂ is an oxide and is not prone to further oxidation upon contacting the SnO₂. This results in stable low-resistance ohmic contacts on the SnO₂ nanobelts. Next, a thin layer of gold was deposited on top of the RuO₂ to help ease wire attachment, and the final device was obtained after liftoff.

A scanning electron microscopy image of a SnO₂ single-nanobelt sensor device is shown in Fig. 1(a). There are four electrical contacts on the nanobelt in order to facilitate precise determination of the resistance and ohmicity of the contacts. For three-terminal FET measurements the center two leads are used as the source/drain contacts. A transmission electron microscopy image of a tin dioxide nanobelt is presented in Fig. 1(b). The contrast lines in Fig. 1(b) are due to strain in

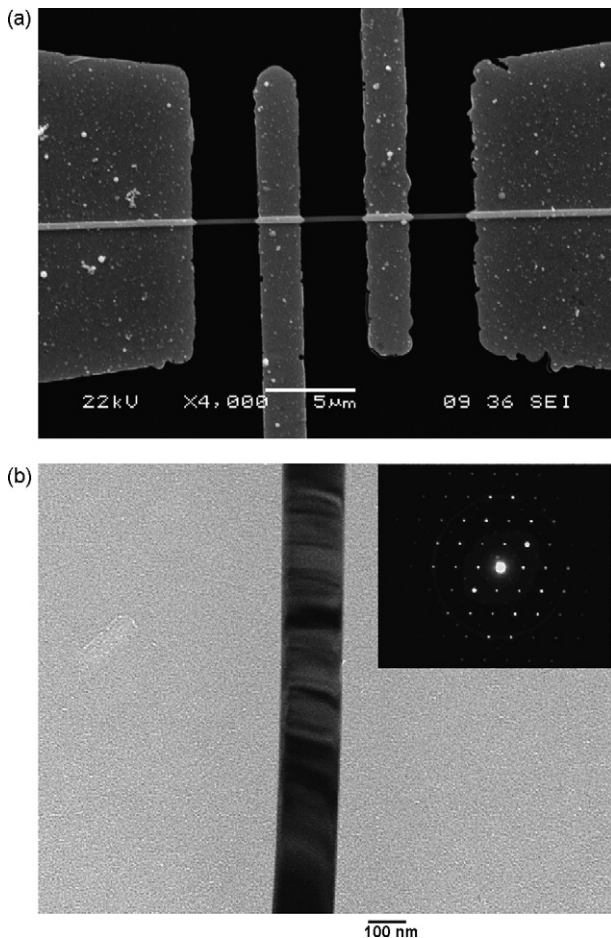


Fig. 1. (a) Scanning electron microscopy image of a tin dioxide sensor of 5 µm channel length; (b) transmission electron microscopy image of a tin dioxide nanobelt. The inset in (b) is a TEM electron diffraction pattern showing that the nanobelt is a single crystal.

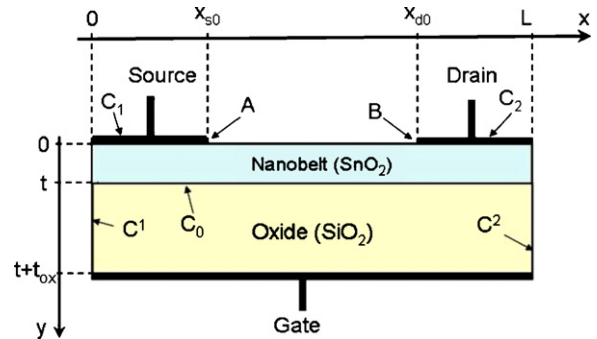


Fig. 2. Two-dimensional schematic representation of the SnO₂ single-nanobelt FET device used in simulations.

the nanobelt. The nanobelt is single-crystalline as verified by the electron diffraction pattern shown in inset of Fig. 1(b). The length of the nanobelt channel between the source/drain terminals is about 20 µm. The width of the nanobelt is about 330 nm and its thickness about 80 nm as determined from atomic force microscopy. Heavily doped n-type silicon was used as a back gate for the device with a 250 nm thick SiO₂ as the gate dielectric. Fig. 2 presents a two-dimensional schematic representation of the device. As seen in this figure, the device is similar in structure to a back-gated metal-oxide-semiconductor field-effect transistor (MOSFET), in which the metal-to-semiconductor interface replaces the MOSFET's metal-to-p-n junction interface at both the source and drain terminals.

The current–voltage characteristics were measured under various ambient conditions. Fig. 3(a and b) shows the measured output characteristics (drain-to-source current versus drain-to-source voltage) of the sensor in air, at 25 and 80 °C, respectively. In these figures the gate voltage is varied from –10 to +10 V in steps of 4 V. It is important to note that the device does not obey the conventional output characteristics of MOSFET devices, where saturation occurs at:

$$V_{DS,sat} = V_{GS} - V_T, \quad (1)$$

where V_T is the threshold voltage, and V_{DS} and V_{GS} are the drain and gate-to-source voltages, respectively. In Fig. 3(a and b), the gate voltage varies from –10 to +10 V, and, according to Eq. (1), the saturation voltage should change by 20 V. However, the saturation voltage is changed by less than a couple of volts when the gate voltage is varied from –10 to 10 V and actually appears to slightly decrease with increasing gate potential (especially at the negative gate potentials). As it will be shown in Section 4 by using numerical simulations and in Appendix A using analytical estimations, pinch-off voltage V_p is larger than 100 V for our FET structure.

The measured output characteristics when H₂ gas is introduced in the system are shown in Fig. 4(a and b) at 25 and 80 °C, respectively. Hydrogen was mixed with nitrogen to form the 2% H₂ gas mixture, which was flowed through a process tube that was heated to the respective temperatures. It is apparent from these measurements that the sensor behaves like a linear resistor, whose resistance is modulated by the back gate potential. Four-point measurements indicate that the contact resistance is indeed much smaller than the bulk resistance of the nanobelt.

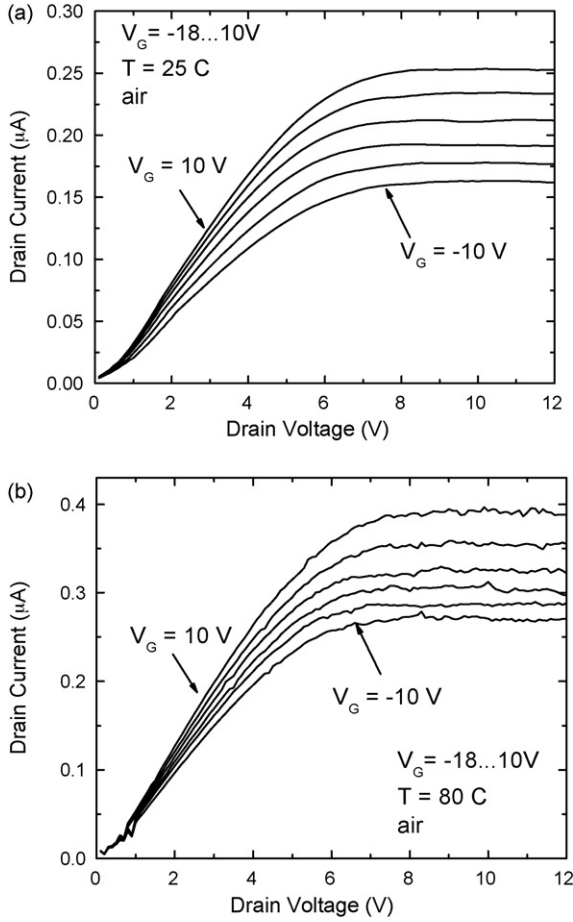


Fig. 3. Measured voltage–current characteristics of the FET device in air at (a) room temperature and (b) $T = 80^\circ\text{C}$. Gate voltage is varied from 10 (top) to -10 V (bottom) in 4 V steps.

3. Model description

Stoichiometric tin dioxide is a metal-oxide semiconductor with a direct bandgap of 3.7 eV. The electronic transport in the tin dioxide sensor can be described by the Poisson equation coupled with the continuity and density-gradient equations [13]:

$$\nabla \cdot (\varepsilon \nabla \varphi) + q(p - n + N_D^+ - N_A^-) = 0, \quad (2)$$

$$\nabla \cdot (\mu_n n \nabla \phi_n) = -R_n, \quad (3)$$

$$\nabla \cdot (\mu_p p \nabla \phi_p) = R_p, \quad (4)$$

$$\frac{2\nabla \cdot (b_n \nabla \sqrt{n})}{\sqrt{n}} + \varphi - \phi_n - \Phi_n(T) = 0, \quad (5)$$

$$\frac{2\nabla \cdot (b_p \nabla \sqrt{p})}{\sqrt{p}} - \varphi + \phi_p + \Phi_p(T) = 0, \quad (6)$$

where φ is the electric potential, n , μ_n , ϕ_n , R_n and p , μ_p , ϕ_p , R_p are the concentrations, mobilities, quasi-Fermi potentials, and net recombination rates of the electrons and holes, respectively. In Eq. (2), N_D^+ and N_A^- are the concentrations of the ionized donor and acceptor impurities, ε the permittivity of the semiconductor, and q is the absolute value of the electron charge. Functions $\Phi_n(T)$ and $\Phi_p(T)$ depend on the nature of the electron

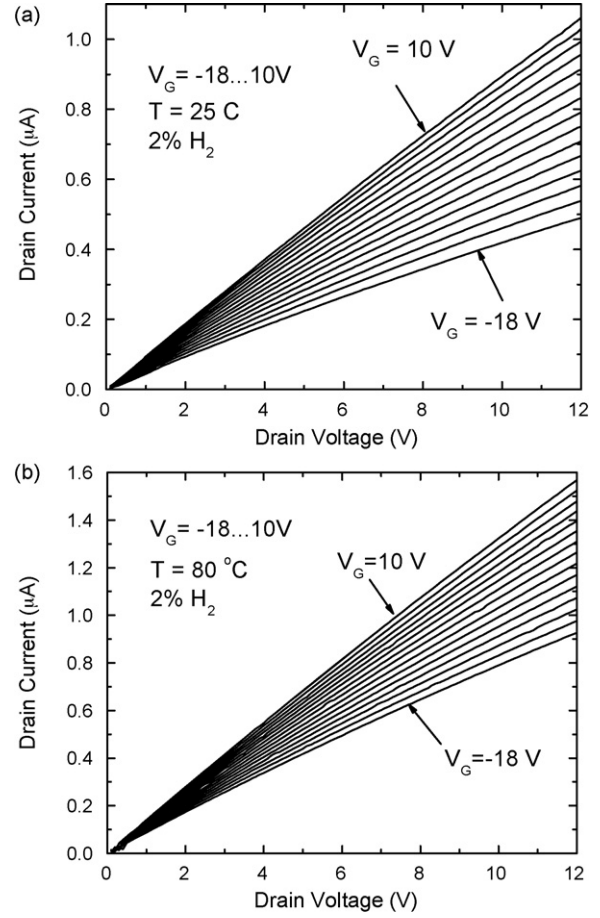


Fig. 4. Measured voltage–current characteristics of the FET device in 2% hydrogen surrounding atmosphere, at (a) room temperature and (b) $T = 80^\circ\text{C}$. Gate voltage is varied from 10 (top) to -18 V (bottom) in 2 V steps.

and hole statistics used. For Fermi statistics $\Phi_n(T)$ and $\Phi_p(T)$ are computed by numerically solving the following equations:

$$n = \frac{2N_c}{\sqrt{\pi}} F_{1/2} \left[\frac{q(\phi_n - \varphi_n)}{kT} \right], \quad (7)$$

$$p = \frac{2N_v}{\sqrt{\pi}} F_{1/2} \left[-\frac{q(\phi_p - \varphi_p) + E_G}{kT} \right], \quad (8)$$

where N_c and N_v are the effective densities of states in the conduction and valence bands, respectively, E_G the bandgap, and $F_{1/2}$ is the Fermi integral of order 1/2. Parameters b_n and b_p in the density-gradient Eqs. (5) and (6) are introduced to account for quantum confinement effects in the semiconductor device. It is assumed that [14]:

$$b_n = \frac{\hbar^2}{12qm_n^*}, \quad b_p = \frac{\hbar^2}{12qm_p^*}, \quad (9)$$

where m_n^* and m_p^* denote the effective masses of the electrons and holes and $\hbar = h/2\pi$, where h is the Planck constant. Note that, if b_n and b_p are set to zero, Eqs. (5) and (6) degenerate into the classical drift-diffusion model. In our simulations, we have used $m_n^* = 0.16m_0$ and $m_p^* = m_0$, where m_0 is the free electron mass, in agreement with the values reported in [15] for carrier concentrations less than 10^{18} cm^{-3} .

Eqs. (2)–(9) are subject to appropriate boundary conditions that depend on the actual geometry of the sensor (see Fig. 2). In our simulations we use Dirichlet boundary conditions at the source and drain contacts (C_1 and C_2), Neumann boundary conditions at the artificial boundaries (C^1 and C^2), and mixed type boundary conditions at the semiconductor–oxide interface (C_0). At the semiconductor–oxygen/hydrogen interface we consider a fixed-charge layer whose concentration depends on the concentration of the hydrogen in the vicinity of the SnO_2 surface. Eqs. (2)–(9) together with the boundary conditions are discretized and solved numerically in two-dimensions by using the finite difference approximation [16]. The density currents at the source and drain electrodes are computed as:

$$j = -q(\mu_n n \nabla \phi_n + \mu_p p \nabla \phi_p). \quad (10)$$

Although the tin dioxide sensor is an unipolar device and holes can be neglected in the bulk conductivity, the hole density current might be important when a high density of negative ions is absorbed at the surface. Such a case can occur when the surface of tin dioxide is exposed to oxygen or another oxidizing gas. For this reason the hole current may not be neglected in transport Eqs. (4), (6), and (10).

The electron and hole drift mobilities of SnO_2 are assumed to be constant over the range of applied fields and of electron and hole concentrations used in the simulations. The bulk mobility of electrons is assumed to depend on the temperature according to the power law [17]:

$$\mu_n = \mu_{n0} \left(\frac{T}{300 \text{ K}} \right)^{-\gamma}, \quad (11)$$

where μ_{n0} is the bulk mobility at 300 K and γ is a coefficient, which in our simulation was equal to 2 [17]. The relative permittivities of SnO_2 and SiO_2 used in the numerical simulations are also considered constant and equal to 12.2 and 3.9, respectively. The concentration of the ionized donor impurities is computed by using Fermi statistics, in which for simplification we have considered only one donor level situated at 0.6 eV below the bottom of the conduction band [18]. All the other energy levels lying in the bandgap are considered either fully occupied or unoccupied and the electron concentration on these levels does not depend on the temperature. Since tin dioxide is a direct gap semiconductor, direct recombination processes are very likely to occur and the net recombination terms in Eqs. (3) and (4) can be expressed as

$$R_n = R_p = C(np - n_i^2), \quad (12)$$

where C is a proportionality constant and n_i is the intrinsic concentration. The effects of the recombination terms (12) can be neglected in the modeling and simulation of I – V characteristics of tin dioxide since the conduction is given by the majority carriers, but cannot be neglected in applications where the minority carriers are important, such as in p–n junctions.

In order to accurately capture the temperature dependent characteristics of the dioxide, the temperature dependence of the

bandgap should be considered carefully in the model. According to [19] we use

$$E_g = E_{g0} - \alpha T, \quad (13)$$

where $\alpha = 6 \times 10^{-4}$ eV/K and $E_{g0} = 3.7$ eV. The affinity of SnO_2 was taken to be $\chi = 7.3$ eV [20]. Schottky barrier lowering effects induced by image charge in the metal contacts should also be used whenever the drain and source junctions are rectifying. The following empirical formula was used to describe Schottky effects:

$$\Delta \Phi = \beta \sqrt{\frac{qE}{4\pi\epsilon}}, \quad (14)$$

where β is an adjustable parameter. Due to the lack of available data in the literature we used the theoretical $\beta = 1$ given by Sze [21]. E is the electric field at the interface and ϵ is the permittivity of SnO_2 .

It is important to note that the doping concentration in tin dioxide is given by the concentration of oxygen vacancies in SnO_2 . The doping profile of the nanobelt might slightly change as a function of the type and concentration of the gas at the surface of the nanobelt. When oxygen comes in the proximity of the nanobelt, oxygen atoms will fill in some of vacancies and so decrease the effective doping concentration in the region close to the surface of the nanobelt. When hydrogen comes in the surrounding atmosphere it will react with the existing oxygen atoms from the dioxide and increase the concentration of the oxygen vacancies in regions close to the surface of the nanobelt. This increase of the doping concentration results in a decrease of the width of the potential barrier at the contacts, and, if the concentration of the hydrogen gas is large enough, electrons will easily tunnel through the barrier, making the contacts look ohmic. The chemical reaction at the SnO_2 surface with H_2 was discussed in our previous paper [9]. However, it should be noted that there might also exist other causes that result in the modification of the nature of the contact from rectifying to ohmic. One of the most important causes is the presence of interface (surface) charges created by atoms of the gas to be detected. Surface states usually can create depletion regions in the semiconductor, as well as dipoles at the metal semiconductor interface. Both effects result in a modification of the electron affinity of the semiconductor and, as a result, of the barrier height at the drain and source contacts [22,23]. The change in the barrier height at the contacts could in principle be computed if the distribution of the surface states in the gap is known. Due to the lack of quantitative data that exist in the literature about the interface charges and the exact mechanisms that result in the change of contact conductance in the presence of external gas, we model the effects of the hydrogen by modifying the potential barrier at the source and drain contacts. Since it seems unlikely that hydrogen can affect regions of tin dioxide far away from the surface, we consider that the potential barrier is lowered only at points close to the inner corners of the metal and source electrodes (see points A and B in Fig. 2). For instance, in the case of the source electrode, the potential barriers

lowered by:

Source potential barrier lowering (x)

$$= \Delta_{\max} \exp \left[-\frac{(x - x_{S0})^2}{2\sigma^2} \right], \quad \text{for } x < x_{S0}, \quad (15)$$

where Δ_{\max} is the barrier lowering at $x = x_{S0}$, σ the standard deviation of the barrier lowering distribution along the x -direction, and x_{S0} is the x -coordinate of the inner edge of the source electrode. In the case of the drain electrode:

Drain potential barrier lowering (x)

$$= \Delta_{\max} \exp \left[-\frac{(x - x_{D0})^2}{2\sigma^2} \right], \quad \text{for } x > x_{D0}, \quad (16)$$

where x_{D0} is the x -coordinate of the inner edge of the drain electrode. Parameters Δ_{\max} and σ should be carefully calibrated against experimental data. Our simulations show that the I – V characteristics for a large range of variation of the gate voltage do not depend significantly on the values of σ , as long as they are larger than a few nanometers. In the simulations presented in this article we have used $\sigma = 5$ nm but, as mentioned before, a larger value of σ would not change significantly the values of the output characteristics, since the contact resistance is much smaller than the resistance of the nanobelt.

The surface states at the interface between the nanobelt and the external atmosphere can be taken into account by using a surface charge layer with density ρ (measured in C/cm²). In the presence of the charge layer the boundary condition for the electrostatic potential is:

$$\varepsilon_s \nabla \varphi|_{\text{nanobelt}} = \varepsilon_{\text{gas}} \nabla \varphi|_{\text{gas}} + \rho, \quad (17)$$

where ε_s is the permittivity of the thin dioxide, ε_{gas} the permittivity of the external gas in the proximity of the nanobelt, and $-\nabla \varphi|_{\text{nanobelt}}$ and $-\nabla \varphi|_{\text{gas}}$ are the electric fields in the nanobelt and in the air, on each side of the surface of the nanobelt, respectively. When surface states are taken into account, the Poisson equation is solved in both the nanobelt and external gas regions, while the continuity and density-gradient equations are solved only in the nanobelt region. The density of the charge layer ρ depends on the type and concentration of the external gas. For instance, the ionized oxygen from the external atmosphere is usually absorbed during high-temperature deposition and subsequent cooling and creates a negatively charged layer at the surface of the nanobelt. This charge layer will push away the free electrons from the surface creating a depletion region, which will decrease the conductivity of the nanobelt. This effect is usually responsible for the change of the conductivity of thin films (less than a few tens of nanometers) or particulate SnO₂ materials but can be neglected in films relatively thick. In our case the thickness of the nanobelt is 80 nm, the width of the depletion region is of the order of a few nanometers (see [24]), and the surface charge can be neglected. This fact is also supported by the experimental data presented in Fig. 3(b), which shows that the drain-to-source saturation voltage does not obey Eq. (1) and

the saturation of the I – V curves cannot be due to a pinch-off effect.

4. Calibration and simulation results

The model described in the previous section has been implemented numerically and used to simulate the I – V characteristics of the tin dioxide nanobelt sensor. The transport equations consisting of the coupled Poisson, current continuity, and density-gradient equations were discretized by using the two-dimensional finite-difference approximation [21] and solved iteratively by using the Newton technique. It is important to note that by using a two-dimensional approach we tacitly neglected the fringe effects of the electric field at the two edges (in the z -direction) of the nanobelt. In our case this effect should not play a significant role since the width is more than 4 times larger than the height of the nanobelt. However, the fringe effects might play an important role if the width is not much larger than the height of the nanobelt (like in the case of circular nanowires). In this case one should either perform three-dimensional simulations or, as mentioned in [25], account for the fringe effects by using a slightly smaller permittivity for the silicon oxide.

The hole current and generation–recombination processes in the bulk of the nanobelt were neglected in the simulations since they do not affect the I – V characteristics significantly. The parameters that affect these characteristics the most are the bulk (effective-field) mobility at 300 K, the doping concentration profile, and the potential barrier at the metal/semiconductor contacts. These parameters were calibrated by fitting the experimental I – V characteristics to the simulated ones. Due to the importance of the calibration technique, we describe below an approximate method for the identification of the doping concentration, mobility, and barrier heights. The identification method presented below was used to provide an initial guess for the model parameters used in simulations. Afterwards, these parameters were slightly adjusted in order to better fit the experimental data to the self-consistent simulations.

The bulk mobility and the concentration of ionized impurities in the nanobelt can be estimated from the output characteristics of the nanobelt in the presence of hydrogen. In this case the contact resistance is much smaller than the channel resistance and the total resistance at low drain voltages can be approximated as:

$$R = \frac{L}{q\mu_n N_d^+ W(t - d)}, \quad (18)$$

where L is the channel length, W the width of the channel, N_d^+ the concentration of the ionized donor levels, and t and d are the thicknesses of the nanobelt and depletion region created by the negative gate voltage in the nanobelt, respectively. By using Eq. (23) (in Appendix A), the derivative of the channel conductance with respect to the gate voltages is:

$$\frac{d(1/R)}{dV_G} = \frac{\mu_n W \varepsilon_{\text{ox}}}{2L} \left(\frac{\varepsilon^2 t_{\text{ox}}^2}{4\varepsilon_{\text{ox}}^2} - \frac{\varepsilon_{\text{ox}}}{qN_d^+} V_G \right)^{-1/2}. \quad (19)$$

which implies that the bulk mobility can be computed using the channel conductance at $V_G = V_D = 0$ as:

$$\mu_n = \frac{L \varepsilon t_{\text{ox}}}{\varepsilon_{\text{ox}}^2} \left. \frac{d(1/R)}{dV_G} \right|_{V_G=V_D=0} \quad (20)$$

By using the last equation we found that the bulk electron mobility of SnO_2 is approximately $6.9 \text{ cm}^2/\text{V s}$, which turns out to be relatively close to the value computed by fitting the experimental data to the numerical solution of Eqs. (2)–(6) and which was found to be $7.5 \text{ cm}^2/\text{V s}$. The concentration of the ionized doping impurities can then be computed by solving numerically:

$$N_d^+ = \frac{L}{q \mu_n W t} \left. \frac{1}{R} \right|_{V_G=V_D=0}, \quad (21)$$

where t is the thickness of the nanobelt. It should be noted that this technique can also be generalized for the computation of the distribution of the concentration of the ionized doping impurities as a function of y , $N_d^+(y)$, since only the impurities at the edge of the depletion region are responsible for the conductance change for a given value of the gate voltage. The concentration of ionized impurities was found to be $N_d^+ = 3.3 \times 10^{17} \text{ cm}^{-3}$ at $T = 25^\circ\text{C}$ and $N_d^+ = 5.3 \times 10^{17} \text{ cm}^{-3}$ at $T = 80^\circ\text{C}$.

In Fig. 5(a and b) we present the I – V characteristics simulated by using the model presented in the previous section when the concentration of the hydrogen is 2%. A very good agreement is observed between these results and the experimental data presented in Fig. 4(a and b).

In ambient air, the drain and source metal contacts have a strong rectifying behavior, which can be observed in the experimental data presented in Fig. 3(a and b). It is important to note again that the saturation of the output characteristics is not due to the pinch-off effects, as Eq. (24) predicts much higher values for the drain-to-source saturation voltage than those observed experimentally. For instance, at $V_G = 0$, the predicted value of the drain-to-source saturation voltage is over 100 V, while experimentally the saturation was observed at approximately 6 V.

By fitting the experimental and simulated output characteristics of the nanobelt in air we have obtained that the potential barrier at the metal/semiconductor contacts is $\Delta_{\text{max}} = 0.378 \text{ eV}$. The simulated output characteristics are presented in Fig. 6(a and b) for $T = 25$ and 80°C . The slight disagreement between the simulated and experimental data at low drain voltages we think is due to second-order effects that are not considered carefully in our model. For instance, at negative gate voltages the electric field at the mobility degradation at interfaces can play an important role and reduce the drain current. Fixed-charges and other impurities might accumulate at the surface of tin dioxide that is in contact with the external gas (not at the tin dioxide/metal contacts) and also create an additional electric field which can modify the electronic conduction in the channel.

In order to compare the effects of the Schottky contact resistance versus the bulk resistance of the nanobelt, Fig. 7 presents the currents through the $20 \mu\text{m}$ SnO_2 nanobelt in two

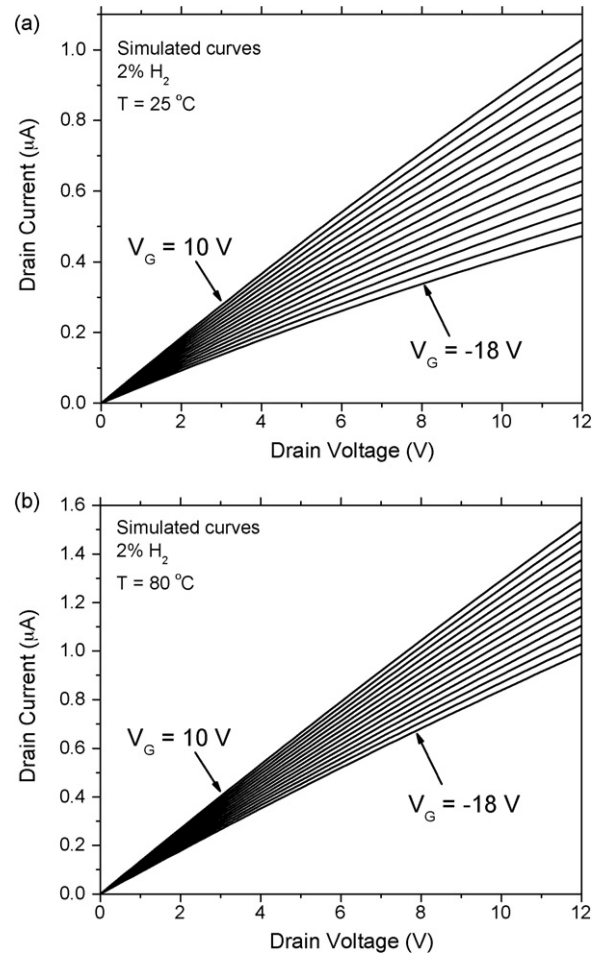


Fig. 5. Simulated voltage–current characteristics of the FET device in 2% hydrogen surrounding atmosphere, at (a) room temperature and (b) $T = 80^\circ\text{C}$. Gate voltage is varied from 10 (top) to -18 V (bottom) in 2 V steps.

cases: (1) only the resistance of the nanobelt is considered in the plot represented by a dashed line and the contacts were assumed ohmic and (2) the resistance of the region nanobelt between source and drain was set to zero and the contacts were treated as Schottky contacts with finite resistance in the plot represented by a continuous line. One can observe that if the drain-to-source voltage is less than approximately 3 V the bulk resistance dominates, while for drain-to-source voltages larger than 3 V the contact resistance dominates. That means that if the nanobelt sensor is biased with $V_{\text{DS}} < 3 \text{ V}$ the resistance of the sensor is mostly given by the interaction of the external gas with the surface of the nanobelt and the contacts do not play a significant role. If $V_{\text{DS}} > 3 \text{ V}$ the resistance of the sensor is mostly given by the resistance of the source and drain Schottky contacts. Since the current through the nanobelt depends exponentially on the barrier height at the metal–nanobelt contacts and the barrier height strongly depends on the type and composition of the external gas [see formulas (15) and (16)], our results suggest that one can possibly build highly sensitive sensors based on the metal-oxide semiconductor Schottky contacts.

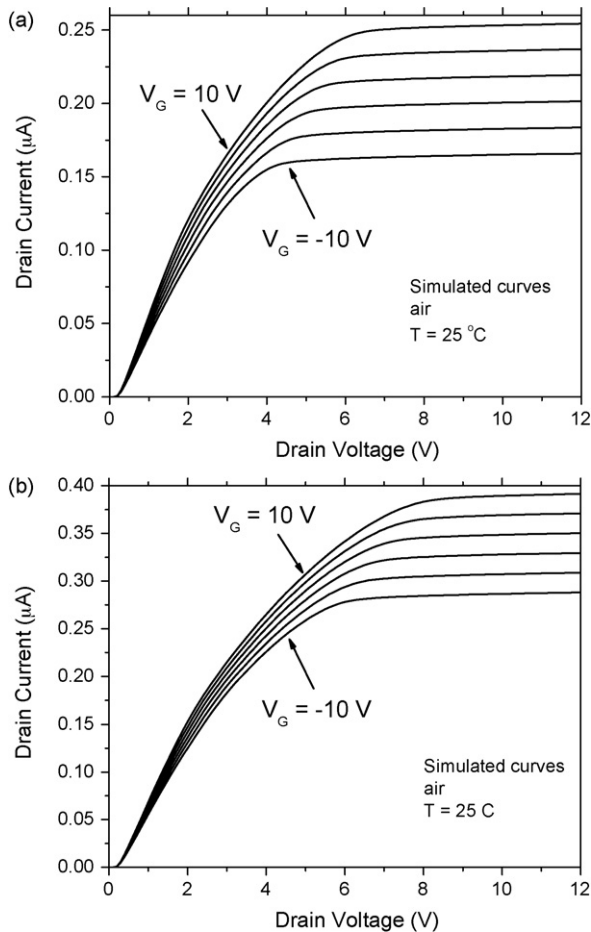


Fig. 6. Simulated voltage–current characteristics of the FET device in air at (a) room temperature and (b) $T = 80^\circ\text{C}$. Gate voltage is varied from 10 (top) to -10 V (bottom) in 4 V steps.

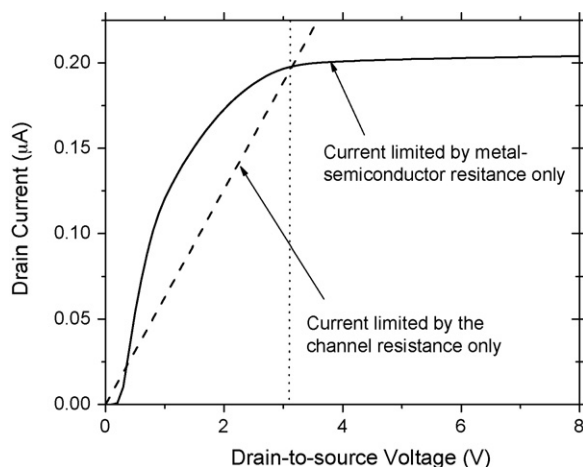


Fig. 7. Current through the nanobelt as computed by considering only the channel resistance (dash line) and the contact resistance (continuous line). Above $V_d = 3\text{ V}$ the contact resistance dominates and the sensitivity of the sensor is dictated by how sensitive the source and drain contacts are to changes in the composition and type of the external gas.

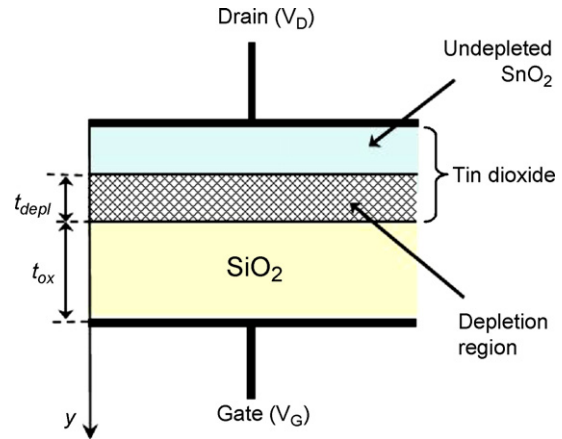


Fig. 8. Representation of the depletion region induced by negative potential on the gate with respect to the drain potential. The pinch-off voltage is given by Eq. (24).

5. Conclusion

It is shown that the pinch-off effect observed when the sensor is in air is not responsible for the saturation of the output characteristics of the SnO_2 FET devices. Rather, the observed saturation is due to the saturation of the reverse-biased Schottky-like contact. The nature of the contact can be changed if hydrogen is introduced in the surrounding atmosphere. A physics-based model based on the Poisson and drift-diffusion equations is presented and used to simulate our FET structures. A very good agreement is observed at various temperatures between the measured output characteristics and the simulated ones.

Acknowledgement

This research was supported by US Army Research Laboratory under Cooperative Agreement DAAD19-01-2-0014.

Appendix A. Computation of pinch-off voltage

The pinch-off voltage of the MOSFET structure presented in Fig. 2 can be computed analytically by assuming that the length of the nanobelt is much larger than the thickness of the nanobelt and the electrostatic potential varies much slower in the direction parallel to the channel than in the direction perpendicular to the channel. Indeed, for our device, the channel length is more than two orders of magnitude larger than the thickness of the nanobelt and one can solve the one-dimensional Poisson equation in the direction perpendicular to the belt directly. When one applies a negative potential on the gate with respect to the source and drain electrodes, a depletion region will appear in the proximity of the $\text{SnO}_2/\text{SiO}_2$ interface (see Fig. 8). The width of the depletion region increases when the potential difference between the drain and the gate electrodes is increased. At pinch-off, the depletion region will touch the metal electrode and will saturate the output characteristics of the sensor.

The one-dimensional Poisson equation in the y-direction:

$$\frac{d^2\varphi}{dy^2} = \begin{cases} 0, & \text{for } 0 < y < t - d, \\ \frac{-qN_d^+}{\varepsilon}, & \text{for } t - d < y < t, \\ 0, & \text{for } t < y < t + t_{ox}, \end{cases} \quad (22)$$

where φ is the electrostatic potential, t and t_{ox} the thicknesses of tin and silicon dioxides, respectively, q the absolute value of the electron charge, ε the permittivity of tin dioxide, d the width of the depletion region created by the gate electrode, and N_d^+ is the concentration of ionized impurities, which is assumed to be constant in the semiconductor. Eq. (22) can be integrated by assuming continuity of the electrostatic potential and of the displacement vector εE (where E is the electric field) at $y = t - d$ and $y = t$. By performing the integration in Eq. (22) one gets the following equation for the width of the depletion region:

$$d = \frac{t_{ox}}{2} \left[-\frac{\varepsilon}{\varepsilon_{ox}} + \sqrt{\frac{\varepsilon^2}{\varepsilon_{ox}^2} + \frac{4\varepsilon_{ox}}{qN_d^+t_{ox}^2}(V_D - V_G)} \right], \quad (23)$$

where ε_{ox} is the permittivity of the SiO_2 , V_D and V_G are the potentials on the drain and source electrodes, respectively. The pinch-off voltage can be computed by setting $d = t$, i.e. the gate potential completely depletes the semiconductor region:

$$V_P = \frac{qN_d^+t}{\varepsilon_{ox}} \left(t + \frac{\varepsilon t_{ox}}{\varepsilon_{ox}} \right). \quad (24)$$

For doping concentrations larger than $3 \times 10^{17} \text{ cm}^{-3}$ the pinch-off voltage is above 100 V.

References

- [1] C.N. Tsai, J.C. Chou, T.P. Sun, S.K. Hsiung, Study on the time-dependent slow response of the tin oxide pH electrode, *IEEE Sens. J.* 6 (2006) 1243–1249.
- [2] E. Comini, L. Ottini, G. Faglia, G. Sberveglieri, SnO_2 RGTO UV activation for CO monitoring, *IEEE Sens. J.* 4 (2004) 17–20.
- [3] M.S. Arnold, P. Avouris, Z.W. Pan, Z.L. Wang, Field-effect transistors based on single semiconducting oxide nanobelts, *J. Phys. Chem. B* 107 (2003) 659–663.
- [4] A. Kolmakov, D.O. Klenov, Y. Lilach, S. Stemmer, M. Moskovits, Enhanced gas sensing by individual SnO_2 nanowires and nanobelts functionalized with Pd catalyst particles, *Nano Lett.* 5 (2005) 667–673.
- [5] B. Esfandiyarpour, S. Mohajerzadeh, A.A. Khodadadi, M.D. Robertson, Ultrahigh-sensitive tin-oxide microsensors for H_2S detection, *IEEE Sens. J.* 4 (2004) 449–454.
- [6] M. Bogner, A. Fuchs, K. Scharnagl, R. Winter, T. Doll, I. Eisele, Electrical field impact on the gas adsorptivity of thin metal oxide films, *Appl. Phys. Lett.* 73 (1998) 2524–2526.
- [7] C.S. Lao, J. Liu, P.X. Gao, L.Y. Zhang, D. Davidovic, R. Tummala, Z.L. Wang, ZnO nanobelt/nanowire Schottky diodes formed by dielectrophoresis alignment across Au electrodes, *Nano Lett.* 6 (2006) 263–266.
- [8] Y. Cheng, P. Xiong, L. Fields, J.P. Zheng, R.S. Yang, Z.L. Wang, Intrinsic characteristics of semiconducting oxide nanobelt field-effect transistors, *Appl. Phys. Lett.* 89 (2006) (093114/1–093114/3).
- [9] L.L. Fields, J.P. Zheng, Y. Cheng, P. Xiong, Room-temperature low-power hydrogen sensor based on a single tin dioxide nanobelt, *Appl. Phys. Lett.* 88 (2006) (263102/1–263102/3).
- [10] E. Stern, G. Cheng, M.P. Young, M.A. Reed, Specific contact resistivity of nanowire devices, *Appl. Phys. Lett.* 88 (2006) (053106/1–053106/3).

- [11] S.V. Kalinin, J. Shin, S. Jesse, D. Geohegan, A.P. Baddorf, Y. Lilach, M. Moskovits, A. Kolmakov, Electronic transport imaging in a multiwire SnO_2 chemical field-effect transistor device, *J. Appl. Phys.* 98 (2005) (044503/1–044503/3).
- [12] T. Takenobu, T. Takahashi, T. Kanbara, K. Tsukagoshi, Y. Aoyagi, Y. Iwasa, High-performance transparent flexible transistors using carbon nanotube films, *Appl. Phys. Lett.* 88 (2006) (033511/1–033511/3).
- [13] M.G. Ancona, G.J. Iafrate, Quantum correction to the equation of state of an electron-gas in a semiconductor, *Phys. Rev. B* 39 (1989) 9536–9540.
- [14] M.G. Ancona, Equations of state for silicon inversion layers, *IEEE Trans. Electron Dev.* 47 (2000) 1449–1456.
- [15] G. Sanon, R. Rup, A. Mansingh, Band-gap narrowing and band-structure in degenerate tin oxide (SnO_2) films, *Phys. Rev. B* 44 (1991) 5672–5680.
- [16] S. Selberherr, *Analysis and Simulation of Semiconductor Devices*, Springer-Verlag, 1984.
- [17] M. Nagasawa, S. Shionoya, S. Makishima, Electron effective mass of SnO_2 , *J. Phys. Soc. Jpn.* 20 (1965) 1093.
- [18] J.E. Houston, E.E. Kohnke, Photoelectronic analysis of imperfections in grown stannic oxide single crystals, *J. Appl. Phys.* 36 (1965) 3931–3938.
- [19] E.E. Kohnke, Electrical and optical properties of natural stannic oxide crystals, *J. Phys. Chem. Solids* 23 (1962) 1557–1562.
- [20] M.N. Islam, M.O. Hakim, Electron-affinity and work function of polycrystalline SnO_2 thin-film, *J. Mater. Sci. Lett.* 5 (1986) 63–65.
- [21] S.M. Sze, *Physics of Semiconductor Devices*, second ed., John Wiley & Sons, 1981.
- [22] T. Sahm, A. Gurlo, N. Barsan, U. Weimar, L. Madler, Fundamental studies on SnO_2 by means of simultaneous work function change and conduction measurements, *Thin Solid Films* 490 (2005) 43–47.
- [23] D.J. Milliron, I.G. Hill, C. Shen, A. Kahn, J. Schwartz, Surface oxidation activates indium tin oxide for hole injection, *J. Appl. Phys.* 87 (2000) 572–576.
- [24] J.E. Dominguez, L. Fu, X.Q. Pan, Effect of crystal defects on the electrical properties in epitaxial tin dioxide thin films, *Appl. Phys. Lett.* 81 (2002) 5168–5170.
- [25] O. Wunnicke, Gate capacitance of back-gated nanowire field-effect transistors, *Appl. Phys. Lett.* 89 (2006) (083102/1–083102/3).

Biographies

P. Andrei received the BS and MS degrees in physics in 1997 and 1999, respectively, both from Alexandru Ioan Cuza University in Romania. In 2004 he received the PhD degree in electrical and computer engineering from the University of Maryland, College Park. Since 2004 he is assistant professor at Florida State University and Florida A&M University. His fields of interest include computational electronics and magnetics, design and optimization of semiconductor devices, noise and fluctuations in nanoscale devices, and the mathematical modeling hysteresis phenomena. He has developed RandFlux and HysterSoft, two software packages for the modeling and simulation of semiconductor devices and magnetic hysteresis.

L.L. Fields received a BS degree in electrical engineering with a minor in physics from Christian Brothers University in Memphis, TN in December of 1988. He worked for the navy full-time as an electronics test engineer from January 1989 until August 2000 and part-time from August 2000 until August 2002. He further continued his education by obtaining a MS degree in electrical engineering from the University of Florida in August of 2002 with focusing on semiconductor devices, semiconductor physics, and circuits, and PhD degree in electrical and computer engineering from FAMU-FSU College of Engineering in August 2006 on dissertation of “The Fabrication, Characterization, and Modeling of a Single Tin Dioxide Nanobelt Chemical Sensor”. In 2006 he joined Corning Co. as a research scientist with continuing research interests in the area of chemical and bio-sensors.

J.P. Zheng received a BS in physics from Fudan University in 1982, MS and PhD in electrical engineering from the State University of New York at Buffalo (SUNY-Buffalo), in 1986 and 1990, respectively. His dissertation covers laser interaction with semiconductors and superconductors. From 1990 to 1992 he was a postdoctoral fellow and research assistant professor at SUNY-Buffalo forcing

on photonic devices. From 1993 to 1997 he worked at US Army Research Laboratory, focusing on energy storage materials and devices. He joined the Electrical and Computer faculty of Florida A&M University and Florida State University in 1997 and currently is a professor with research interests including nanomaterials and devices fabrication and characterization, energy storage materials and devices, solid-state thin film deposition, and optoelectronic devices.

Y. Cheng received a bachelor's degree in applied physics from Anhui University, China, in 2002, performing undergraduate research in nanowire growth by electrodeposition with anodic alumina templates. Since August 2002, he has been a research assistant at the Center for Materials Research and Technology (MARTECH) and Department of Physics at Florida State University, with a PhD in physics expected late 2007. His dissertation research focuses on fabrication, characterization and functionalization of quasi-one-dimensional (Q1D)

binary oxide nanobelt based field-effect transistor (FET) and their chemical and biological sensing applications.

P. Xiong received a BS in physics from University of Science and Technology in 1987 and a PhD in physics from Brown University in 1993, with a thesis covering topics of high temperature superconductivity, magnetic granular solids, and mesoscale superconductivity. From 1993 to 1997 he was a postdoctoral fellow at the University of California at San Diego, performing research in superconductor–insulator transition and fluctuation effects in two- and one-dimensional systems. He joined the Physics faculty of the Florida State University in November of 1997 as a member of the Center for Materials Research and Technology (MARTECH). His current research activities include mesoscale physics, spintronics materials and devices, and organic/solid-state hybrid nanostructures.